Physica B: Condensed Matter 553 (2019) 59–67

Contents lists available at ScienceDirect

Physica B: Condensed Matter

journal homepage: www.elsevier.com/locate/physb

Electronic structure, magnetism, and hyperfine interactions in the $EuRhO_3$ orthorhodite

Farshad Nejadsattari[a], Zbigniew M. Stadnik[a,*], Yujiro Nagata[b], Tomohiro Ohnishi[c]

[a] Department of Physics, University of Ottawa, Ottawa, Ontario K1N 6N5, Canada
[b] College of Science and Engineering, Aoyama Gakuin University, Fuchinobe, Sagamihara, Kanagawa 157-8572, Japan
[c] Department of Chemical Engineering, Faculty of Engineering, Kyushu University, Japan

ARTICLE INFO

Keywords:
Paramagnet
^{151}Eu Mössbauer spectroscopy
Electric quadrupole interaction
Electronic structure
Density of states
Debye temperature

ABSTRACT

The results of *ab − initio* electronic structure calculations, X-ray diffraction, magnetic, and ^{151}Eu Mössbauer spectroscopy investigations of the $EuRhO_3$ orthorhodite are presented. The orthorhodite is shown to crystallize in the orthorhombic space group *Pnma* and its lattice constants are $a = 5.7499(1)$ Å, $b = 7.6863(1)$ Å, and $c = 5.3095(1)$ Å. The electron charge density distributions point toward the presence of a mixture of ionic and directional covalent bonding. A detailed analysis of the density of states and the energy band structure reveals half-metallic/half-insulator characteristics of $EuRhO_3$. The Eu atoms in $EuRhO_3$ are shown to be in the trivalent oxidation state. It is demonstrated that $EuRhO_3$ is a paramagnet down to 2.3 K. The Debye temperature of $EuRhO_3$ is found to be 254(3) K.

1. Introduction

The perovskite-type oxides are the compounds of the chemical formula ABO_3, in which A and B correspond to large and small cations, respectively. These compounds have been widely studied. Rare-earth (R) orthorhodites, $RRhO_3$, constitute a subset [1] of the ABO_3 oxides and the physical properties only of a few of them (*vide infra*) have been investigated.

It was found that the $LuRhO_3$ orthorhodite is a *p*-type semiconductor and that it acts as a good hydrogen reduction catalyst [2]. No magnetic ordering of this orthorhodite was observed down to 2.0 K [3]. The Debye temperature of $LuRhO_3$ was found to be 271 K [3]. The semiconductor behavior of other $RRhO_3$ orthorhodites (R = La, Nd, Sm, Eu, Gd, Dy, Er, and Lu) [4] was inferred from their temperature dependence of the electrical resistivity. The results of the magnetic, specific heat, and ^{155}Gd Mössbauer spectroscopy measurements of the $RRhO_3$ orthorhodites (R = rare-earth except Ce and *Pm*) demonstrated that they exhibit either a long-range antiferromagnetic ordering or are paramagnets [4–6].

The purpose of this work is to investigate structural, electronic, magnetic, and hyperfine-interaction properties of the $EuRhO_3$ orthorhodite. To explore these properties, X-ray diffraction, magnetic, and ^{151}Eu Mössbauer spectroscopy experimental techniques and the first-principles electronic structure calculations are used.

2. Experimental and theoretical methods

The polycrystalline $EuRhO_3$ sample was synthesized by the solid-state reaction, following the procedure described in Ref. [4].

The room-temperature X-ray diffraction spectrum was measured with a PANalytical X'Pert scanning diffractometer. The spectrum was collected in the 2θ range 15–85°, in steps of 0.02°, using Cu $K\alpha$ radiation. A Kevex PSi2 Peltier-cooled solid-state Si detector was used to eliminate the $K\beta$ line.

Quantum Design (QD) Magnetic Property Measurement System was employed to measure the dc magnetic susceptibility in the temperature range 1.8–300 K.

The methodology of the ^{151}Eu Mössbauer [7] measurements is the same as that described in Ref. [8]. Here the surface density of the Mössbauer absorber used was 42.8 mg/cm^2, which corresponds to an effective thickness parameter [7] t_a of $9.67f_a$, where f_a is the Debye-Waller factor of the absorber. Because $t_a > 1$, a transmission integral formula [9] was used to described the resonance line shape of the Mössbauer spectra.

We carried out *ab initio* electronic structure calculations using the implementation of density functional theory (DFT) provided by the full-potential linearized augmented-plane-wave plus local orbitals (FP-LAPW + lo) method employed in the WIEN2k package [10]. This method is described in detail in Ref. [6]. Here, the values of 2.21, 2.03, and 1.74 a.u. were used as the muffin-tin sphere radii for Eu, Rh, and O,

* Corresponding author.
E-mail address: stadnik@uottawa.ca (Z.M. Stadnik).

https://doi.org/10.1016/j.physb.2018.10.022
Received 13 September 2018; Accepted 15 October 2018
Available online 23 October 2018

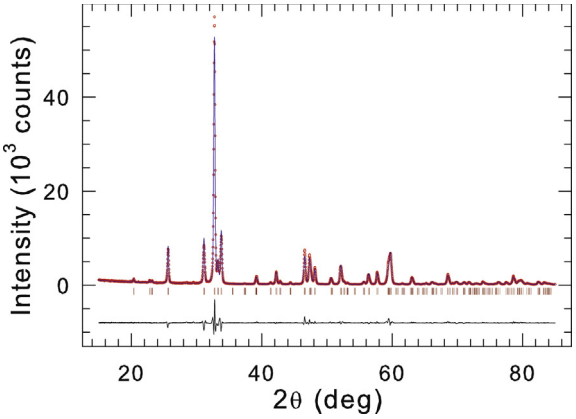

Fig. 1. The X-ray powder diffraction spectrum of $EuRhO_3$ at 298 K. The experimental data are denoted by open circles, while the line through the circles represents the result of the Rietveld refinement. The row of vertical bars represents the Bragg peak positions for the *Pnma* space group. The lower solid line represents the difference curve between experimental and calculated spectra.

respectively. We used 245 inequivalent k-points within a $13 \times 10 \times 14$ k-mesh in the irreducible wedge of the first Brillouin zone. In the calculations, we used the experimental lattice parameters (a, b, and c) and the atomic position parameters in the space group *Pnma* (*vide infra*).

3. Results and discussion

3.1. Structural characterization

A Rietveld refinement [11] of the room-temperature X-ray powder diffraction pattern of $EuRhO_3$ (Fig. 1) confirms that the studied compound crystallizes in the orthorhombic space group *Pnma* (No. 62) [1]. It yields the lattice parameters $a = 5.7499(1)$ Å, $b = 7.6863(1)$ Å, $c = 5.3095(1)$ Å, and the atomic positional parameters that are listed in Table 1. The values of these parameters are close to those reported earlier [1]. No second phase/phases could be detected in the X-ray powder diffraction pattern of $EuRhO_3$ (Fig. 1).

Fig. 2 shows the crystal structure of $EuRhO_3$. The unit cell of $EuRhO_3$ is a cuboid elongated along the b-direction. Consequently, a larger separation between atoms along that direction is related to a weaker electrostatic interaction between them (*vide infra*). Each unit cell (Fig. 2) contains four formula units of $EuRhO_3$. Chemical bonds are expected to be formed between the Eu and Rh atoms with their neighboring O atoms. The connecting rods in Fig. 2 indicate the presence of these bonds. The chemical bonds create an internal network between adjacent atoms. This results in the delocalization of the valence states in the compound studied (*vide infra*). Two types of chemical bonds are observed in $EuRhO_3$: ionic bonds between Eu^{3+} and $[RhO_3]^{3-}$ and covalent bonds between Rh and O atoms. The electronic structure and valence charge density calculations (*vide infra*) enable one to study and discuss the nature of these bonds in the $EuRhO_3$ compound (*vide infra*).

Table 1
Atomic positions for the orthogonal $EuRhO_3$ (space group *Pnma*) obtained through Rietveld analysis and calculated V_{zz} (in units of 10^{21} V/m^2) and η.

Atom	Site	Point symmetry	x	y	z	V_{zz}	η
Eu	4c	$.m.$	0.4242	$\frac{1}{4}$	0.0227	13.39	0.401
Rh	4a	$\bar{1}$	0.0	0.0	0.0	−4.936	0.490
O1	4c	$.m.$	0.5523	$\frac{1}{4}$	0.6440	9.278	0.618
O2	8d	1	0.2037	0.0599	0.3202	10.44	0.251

3.2. Ab − initio calculations

3.2.1. Charge density distributions

A mixture of ionic and covalent bonding exists in $EuRhO_3$. The calculated valence charge density distributions along three different crystallographic planes are shown in Fig. 3. An inspection of Fig. 3(a) reveals the half-metallic and half-insulator characteristics of $EuRhO_3$. One observes parallel conducting sheets composed of alternating Rh and O atoms that are partially separated by the insulating regions that are centered at the Eu atoms. One can conclude that a relatively strong ionic bonding exists between the Eu^{3+} ions and the $[RhO_3]^{3-}$ units. The red regions in Fig. 3(a) indicate an almost complete charge transfer from the Eu 6s orbitals to RhO_3. This can be understood based on the electronegativity argument: there is a significant difference in electronegativity between the Eu (1.20) and the Rh (2.28) and O (3.22) atoms.

The green/cyan regions between the O and Rh atoms [Fig. 3(a)] indicate the charge delocalization in these regions. This is indicative of the presence of directional covalent bonding between these atoms. Within each $[RhO_3]^{3-}$ unit, the O 2p orbitals overlap with the Rh 5s orbitals, forming the directional bonds. This bonding between O and Rh can be also seen along other crystallographic planes [Fig. 3(b) and (c)]. This supports the depiction of the bonds in Fig. 2 by the connecting rods. In addition, a relatively weak covalent bonding between the Eu and O atoms can be observed in Fig. 3(a). One can thus conclude that the interaction the O and Eu atoms is predominantly ionic rather than covalent. This is confirmed by a relatively spherical charge density distribution at the Eu sites.

The presence of a relatively strong directional covalent bonding between the Rh and O atoms is evident in Fig. 3(b). The cyan-colored bridges that connect the Rh and O atoms indicate a high density of delocalized electrons in these regions. This can be explained by a relatively large spatial extent of the O 2p orbitals. The electronic cloud in these orbitals has a dumbbell-like shape. Consequently, a considerable overlap between these states and the Rh 4d and 5s orbitals is expected. Hence, the valence electrons of Rh and O are shared. The strong $s - p$ and $p - d$ hybridization between the Rh and O atoms results from a relatively small distance between these two atoms. The bridges of charge density form a network-like structure surrounding islands of charge density deficiency (indicated by red color). A careful inspection of the charge density at the O atoms in Fig. 3(b) shows that the covalent bonding between the O and Rh atoms causes a deformation of the electronic cloud at the O atoms from a perfectly spherical shape into an ellipsoid elongated toward the neighboring Rh atoms.

The electron charge density distributions along the (110) plane [Fig. 3(c)] are dominated by red/yellow regions that indicate the virtual absence of the charge density. The insulating nature of the compound studied may result from the presence of these regions. One can state that along the (110) planes $EuRhO_3$ exhibits a minimum metallic behavior. However, one observes a strong directional covalent bonding between the O and Rh atoms [Fig. 3(c)]. Although there is a large number of atoms in the (110) plane, their mutual interactions cause the distribution of the valence electrons such that large areas of the electron deficiency are created (red/yellow regions).

3.2.2. Density of states

An inspection of the total and atom-resolved density of states (DOS) of $EuRhO_3$ [Fig. 4(a)] shows that the main contribution to DOS originates from the Eu and Rh atoms. The Eu contribution to DOS is mainly observed in two energy regions. The first region contains a highly localized peak in the vicinity of the Fermi level. A broad and delocalized Eu contribution to DOS is seen in the second region between 4.5 and 8.8 eV.

The DOS arising from the Rh atoms [Fig. 4(a)] does not significantly overlap with that originating from the Eu atoms, and is less localized. The Rh states are observed in three energy regions. The first one lies deep below the Fermi level, extending from −7.4 to −3.0 eV, and

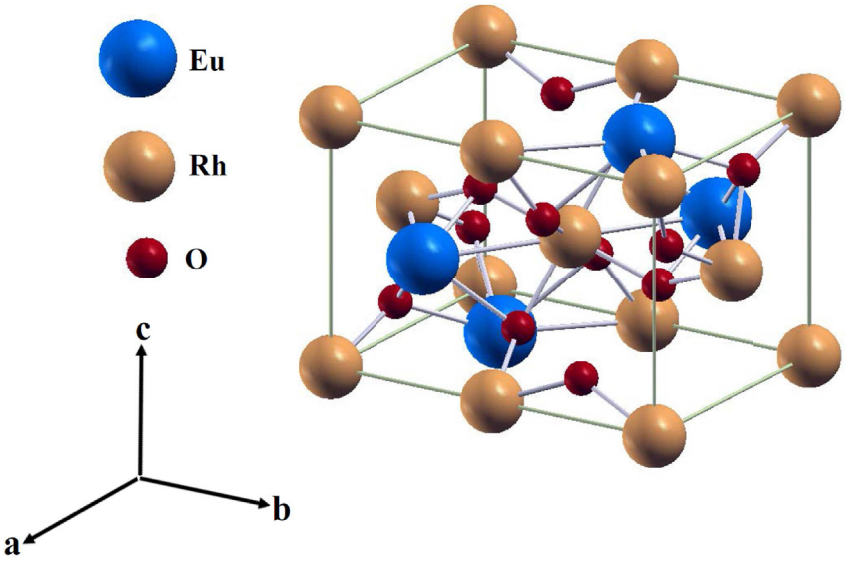

Fig. 2. The unit cell of the $EuRhO_3$ compound.

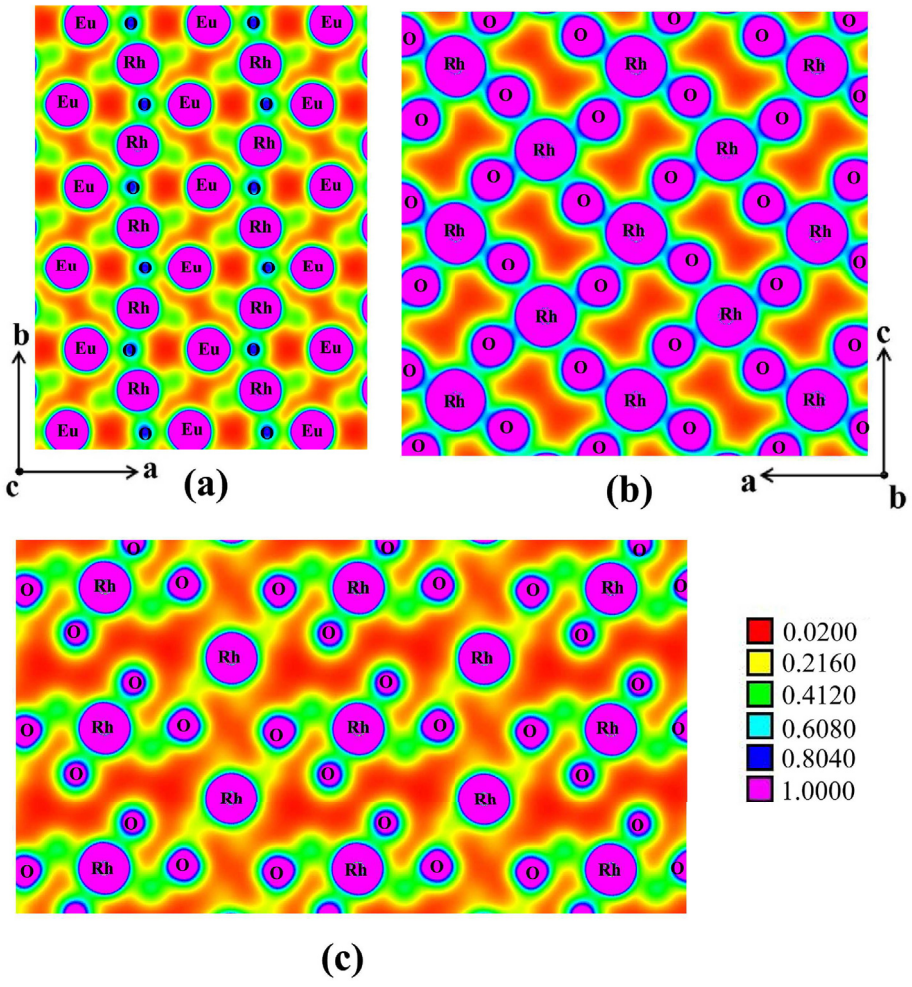

Fig. 3. Electron charge density distributions (in units of e/Å^3) in the (001) plane (a), (010) plane (b), and (110) plane (c).

contains Rh core and semi-core states. These states exhibit atomic-like character and do not contribute to the physical and chemical properties of $EuRhO_3$. The second region extends from −2.8 to −0.7 eV and contains the Rh valence states. The Rh conduction states are located in the third region that is between 0.5 and 3.0 eV.

The contribution to DOS from the O atoms is mainly delocalized below the Fermi level and shows a significant overlap with that from the Rh atoms [Fig. 4(a)]. This can explain the covalent nature of the chemical bonding between these atoms. The dominant O contribution to DOS lies deep in energy in the semi-core and core regions. In the

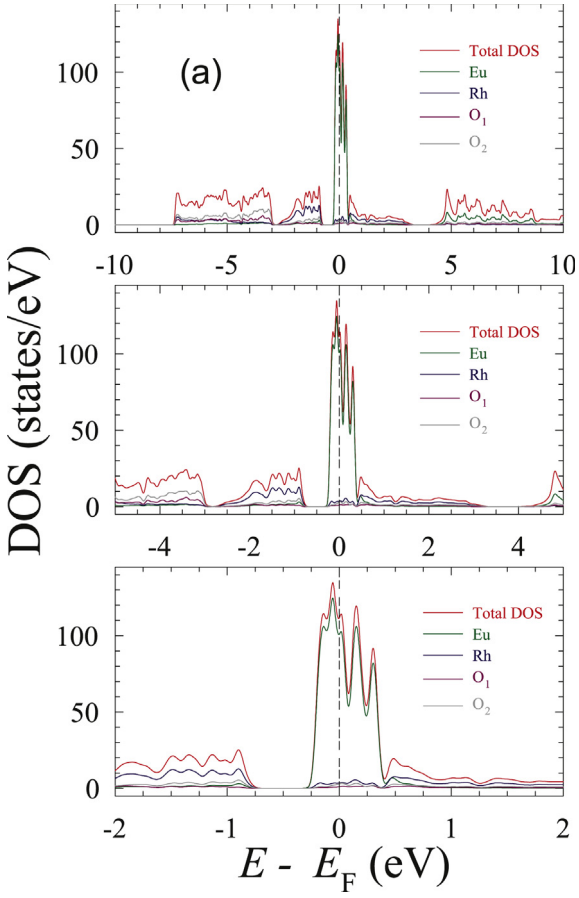

Fig. 4. Total and atom-resolved density of states of $EuRhO_3$ for the energy range between −10 and 10 eV (a), between −5 and 5 eV (b), and between −2 and 2 eV (c).

valence state region (between −2.8 and −0.7 eV), one observes a strong overlap between the O and Rh states, which leads to a $p - d$ hybridization between the Rh 4d and O 2*p* states. This overlap results in the formation of directional covalent bonds between these atoms. There exists a non-zero overlap of the O and Rh states within the Fermi energy region, which explains a small conductivity of the compound studied.

The plot of DOS in a narrower energy region [Fig. 4(b)] shows the highly peaked central area consisting of three peaks originating from the Eu states and a pseudogap in the Eu DOS located immediately above the Fermi level. One also observes two energy gaps: one found in the valence region between −0.7 and −0.2 eV and the other lying high above the Fermi level between 3.3 and 4.1 eV. One notices that the Rh states are also present and are located at different energies than those of the Eu states.

Most of the physical and chemical properties of a compound arise from its DOS structure in the vicinity of the Fermi level. One finds that the Eu states are highly localized in energy and are peaked at −0.5, 0.16, and 0.3 eV [Fig. 4(c)]. Although DOS across the Fermi level is large, this does not necessarily imply high conductivity as these are Eu 4*f* states which are very well localized. The conductive properties of $EuRhO_3$ are the result of the non-zero DOS associated with the Rh and O states that exist between −0.3 and 0.4 eV. The strong ionic bonds between the Eu atoms and the O and Rh atoms can be explained by a negligible overlap between the Eu states and the O and Rh states.

The plot of the orbital-resolved DOS of Eu [Fig. 5(a)] shows that the Fermi-energy region is dominated by the Eu 4*f* states, whereas the energy region between 4.5 and 9.0 eV is occupied by the Eu 4d states. The Eu 4*f* states occupying the region between −0.3 and 0.8 eV are narrow and localized. Hence, they do not contribute to charge transfer.

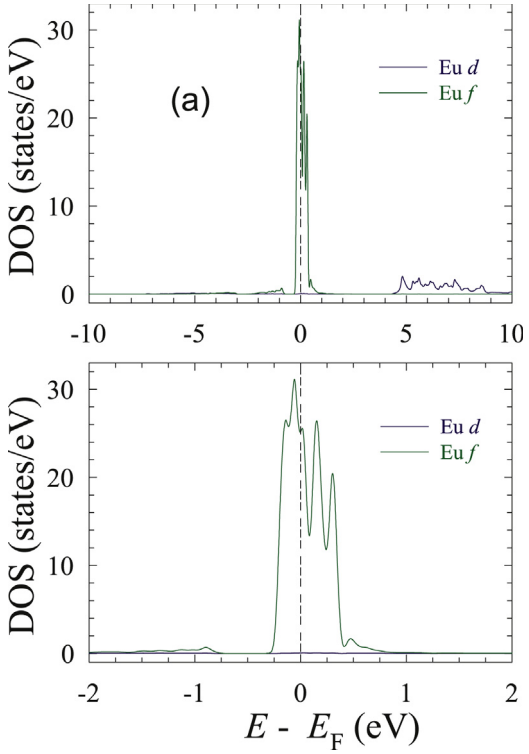

Fig. 5. Orbital-resolved density of states of Eu in $EuRhO_3$ for the energy range between −10 and 10 eV (a) and between −2 and 2 eV (b).

The Eu 4d states, although much broader, lie very high above the Fermi level. Thus, under normal conditions, no charge has enough energy to be excited into these states. Consequently, the insulating behavior of $EuRhO_3$ emerges mainly from the Eu^{3+} ions.

Fig. 5(b) displays the Eu 4*f* orbital contribution to DOS in more detail. As mentioned earlier, the Eu 4*f* states show a number of peaks below and above the Fermi level. Two pseudogaps at 0.08 and 0.24 eVcan also be clearly seen.

The five *d* orbitals contributing to the Rh DOS are to some extent localized [Fig. 6(a)]. However, since they are peaked at different energies, the overall Rh *d* DOS is broad in energy. The d_{z^2} and d_{xy} orbitals are peaked between −1.0 and 2.0 eV. The d_{yz} orbital is peaked at −2.0 eV, and the d_{xz} and, to a lesser extent, the $d_{x^2-y^2}$ orbitals are peaked around 0.5 eV. As one can notice in Fig. 6(b), a mixture of all five *d* orbitals is present around the Fermi level. However, they do not contribute to the majority of the Rh DOS, which again shows a non-conductive feature of the compound studied. The majority of the Rh states are located below the energy gap at −0.7 eV. The conduction states are mainly due to the d_{xz} and $d_{x^2-y^2}$ orbitals which are peaked between 0.4 and 0.8 eV Fig. 6(b).

The major contribution to the O DOS is from the O2 atoms [Fig. 7(a)]. This is related to the Wyckoff positions occupied by the O2 atoms: they are twice as numerous as those occupied by the O1 atoms (Table 1). The occupation and distribution in energy of the O DOS are similar for both O1 and O2 atoms. The O DOS is mainly restricted to four energy regions [Fig. 7(a)]. The first region located between −7.4 and −3.0 eV is the semi-core region. The majority of the O 2*p* states are found in this region. As these states lie deep in energy, they are more atomic-like states and thus do not contribute toward the physical properties of $EuRhO_3$. The second region contains the valence states and is located between −2.8 and −0.8 eV. Two peaks are observed in this region: the larger one at −0.9 eV is associated with the O2 *p* states and the other at −1.8 eV originates from the O1 atoms. The O valence states are separated from the conduction states by a small gap of ~0.5 eV. The conduction states in the third energy region are found in

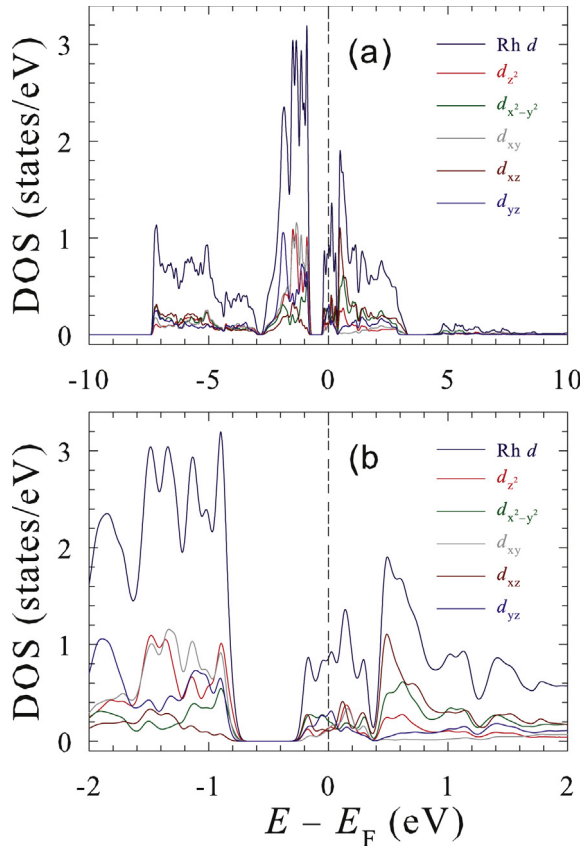

Fig. 6. Total and *d*-orbital-resolved density of states of Rh in $EuRhO_3$ for the energy range between −10 and 10 eV (a) and between −2 and 2 eV (b).

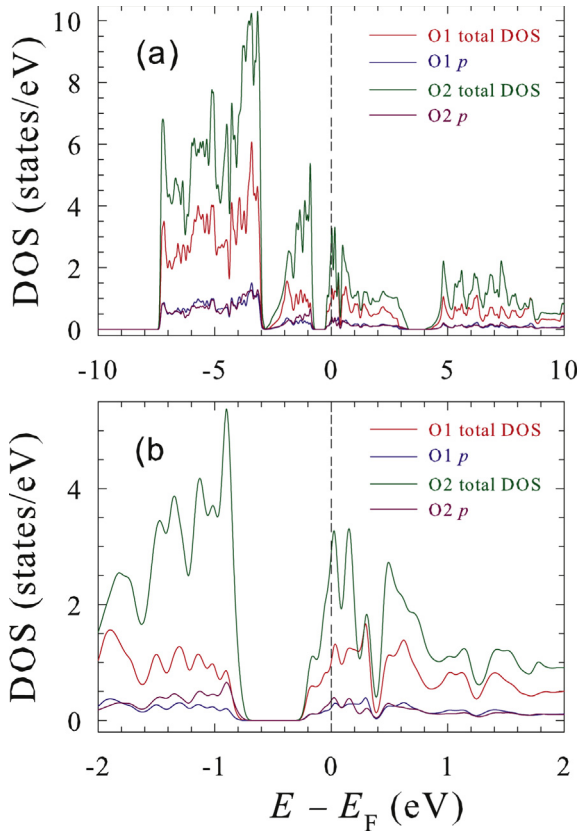

Fig. 7. Total and orbital-resolved density of states of O in $EuRhO_3$ for the energy range between −10 and 10 eV (a) and between −2 and 2 eV (b).

the energy range from the Fermi level to 3.3 eV. The fourth region lies significantly above the Fermi level (between 4.0 and 9.0 eV) and mainly contains the unoccupied states. It is clear from Fig. 7(a) that the main contribution to the O DOS comes from the semi-core region. Within the Fermi region [Fig. 7(b)], one notices the presence of a double-peak feature originating from the O2 states. Again, the non-zero DOS at the Fermi level points toward some conductive behavior of the system studied.

3.2.3. Energy band structure

The features of the electronic structure described above can also be observed in the energy band structure of $EuRhO_3$ (Fig. 8). Five different energy regions can be distinguished [Fig. 8(a)]. The first region starts at 4.0 eV and extends up to 10 eV. The bands in this region correspond to the high-energy, empty states as no electron will have enough energy to be excited into these bands. As these bands are relatively localized, they are mainly of *d* character. In particular, these are the vacant *d* bands originating from the Eu and Rh atoms.

The second energy region is between 0.5 and 3.5 eV [Fig. 8(a)]. The bands in this region are separated from the high-energy bands by a gap that varies from 1.0 eV at the Γ point to 3.5 eV at the M point. This is the realm of the conduction bands. Energetic electrons can be excited into these bands. One observes relatively large energy variations of these bands along various symmetry directions in the Brillouin zone. This corresponds to a larger energy gradient with respect to momentum in the reciprocal space which leads to a larger crystal momentum of the charge carriers that are excited into these states. As a result, higher mobility of the charge carriers is expected. However, as these bands are not numerous, the conduction is relatively low, and the compound is expected to behave more like an insulator.

The third energy region extends from −0.5 to 0.5 eV [Fig. 8(a)] and is packed with highly localized bands of *f* character. These bands appear to be almost flat in the entire Brillouin zone. This indicates that any charge carrier within these bands will have a very high effective mass, which corresponds to an almost zero mobility. Thus, these bands cannot participate in the electronic conduction of $EuRhO_3$.

The fourth energy region lies between −2.8 and −0.8 eV [Fig. 8(a)]. It contains many valence bands which are separated from the flat bands by an energy gap that varies from 0.5 eV at the Γ point to 1.0 eV at the M point. The bands in this region mainly originate from the Rh 5s, 4d and O 2*p* states. These states, via $s - p$ and $p - d$ hybridization, form the aforementioned covalent bonds. The bands in the fourth energy region are less localized in energy and show a relatively strng energy dispersion.

The fifth energy region, the so-called semi-core/core region, is between −7.3 and −3.0 eV. The bands in this region originate mainly from the O atoms and are of atomic character. As mentioned earlier, since these bands are located far below the Fermi level, the corresponding states do not contribute to the physical and chemical properties of $EuRhO_3$.

Fig. 8(b) displays the band structure for the energies between −5.0 and 5.0 eV. We compare here the dispersion relations in the three energy regions described above (second, third, and fourth). It is clear that the conduction and valence bands are highly dispersive in energy. In other words, as one traverses the Brillouin zone across different symmetry points, the bands change rapidly in energy and merge in the high symmetry points, such as Γ, X, and M. The high symmetry of these points causes the states in them to be highly degenerate. The degeneracy is broken as one moves from one high-symmetry point to another. Thus, these bands can potentially contribute to the transport properties of the compound studied. The O 2*p* valence states show a relatively large dispersion along some paths, thus allowing them to share their electrons with those of the neighboring Rh and O atoms. This explains the presence of a relatively high electron-charge concentration in the

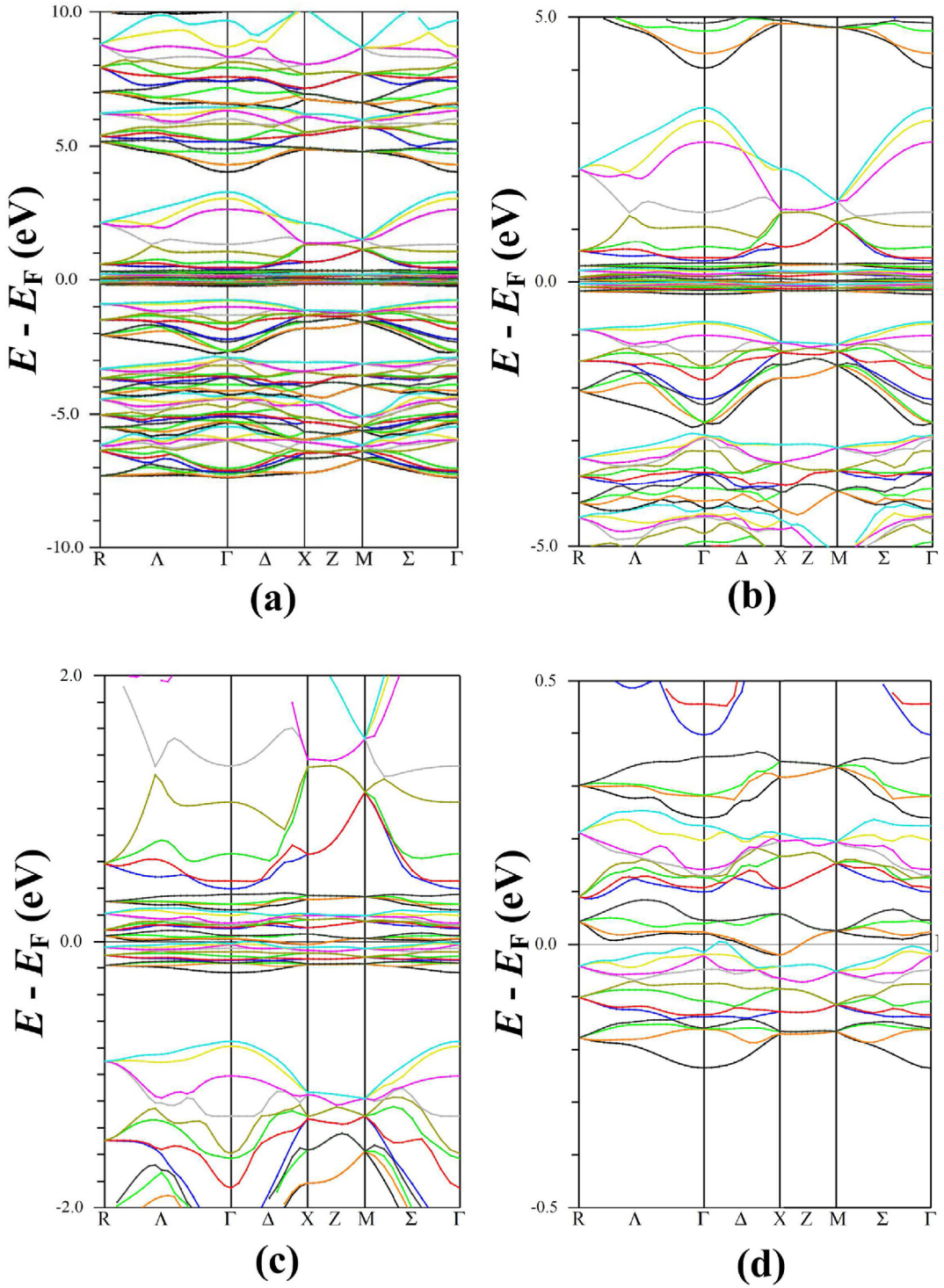

Fig. 8. Energy band structure of $EuRhO_3$ for the energy ranges between −10 and 10 eV (a), −5 and 5 eV (b), −2 and 2 eV (c), and −0.5 and 0.5 eV (d).

regions between these atoms. On the contrary, the numerous flat bands in the Fermi region forbid any type of transport. As mentioned before, the *f* bands are very localized in energy [Fig. 8(b)].

The band structure in the near Fermi region (an energy window between −2.0 and 2.0 eV) is displayed in Fig. 8(c). Most of the physical and chemical properties are determined by the bands in this region. One can notice very slight variations in the "flat" bands mentioned above. One also finds that there are small energy gaps between these bands. In addition to the *f* states, the Rh *s* and O *p* states also contribute to the bands in the near Fermi region.

Fig. 8(d) shows the band structure in the immediate vicinity of the Fermi level (a narrow energy window of 1.0 eV). A careful inspection of this figure reveals that only three bands cross the Fermi level: only along the Γ path from Γ to X in the Brillouin zone. This indicates that although there are many bands in the vicinity of the Fermi level, it is crossed only by these three bands. This also demonstrates that $EuRhO_3$ must be an insulator.

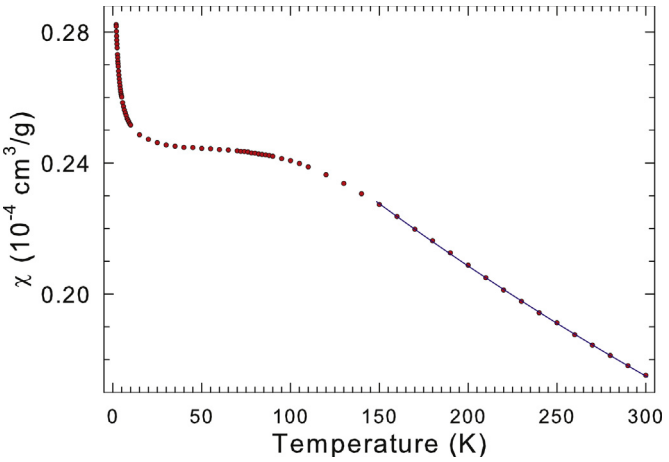

Fig. 9. Temperature dependence of the magnetic susceptibility of $EuRhO_3$, measured in an external magnetic field of 1.0 kOe. The solid line is the fit to Eq. (1) in the temperature range 150–300 K, as explained in the text.

3.3. Calculated Mössbauer parameters

The calculated values of V_{zz} and the asymmetry parameter η [7] at the Eu, Rh, O1, and O2 sites are given in Table 1.

3.4. Magnetic measurements

The temperature dependence of the magnetic susceptibility χ of $EuRhO_3$ measured in an applied magnetic field of 1.0 kOe is displayed in Fig. 9. A sharp upturn of χ below 15 K is probably caused by the presence in the specimen of a tiny amount of a magnetic impurity phase. The absence of a sharp peak in the $\chi(T)$ data indicates the lack of long-range antiferromagnetic order in $EuRhO_3$. The shape of the $\chi(T)$ dependence, excluding the $\chi(T)$ upturn below 15 K, is typical of a Eu^{3+} compound [12,13]. The non-zero Eu^{3+} magnetic moment results from Van Vleck's formula which considers the excited states and not only the ground state [12,13]. Its value is about 3.1–3.6 μ_B in the Eu^{3+} compounds [12,13].

The $\chi(T)$ data above 150 K [Fig. 9] were fitted to a modified Curie-Weiss law

$$\chi = \chi_0 + \frac{C}{T-\Theta_p}. \quad (1)$$

Here χ_0 is the temperature-independent magnetic susceptibility, C is the Curie constant, and Θ_p is the paramagnetic Curie temperature. The Curie constant $C = \frac{N\mu_{eff}^2}{3k_B}$, where N is the number of magnetic moment carrying atoms per formula unit, μ_{eff} is the effective magnetic moment per magnetic atom, and k_B is the Boltzmann constant. The fit yields the following values of χ_0, C, and Θ_p: $-\ 2.19(37) \times 10^{-5}$ cm^3/g, $50.23(8.91) \times 10^{-3}$ cm^3K/g, and $-974(106)$ K. From the value of C one obtains $\mu_{eff} = 7.80(70)$ μ_B per magnetic atom (Eu,Rh). The negative value of Θ_p shows that the interaction between the spins is mainly antiferromagnetic.

3.5. Mössbauer spectroscopy

The ^{151}Eu Mössbauer spectra of $EuRhO_3$ at selected temperatures between room and liquid-helium temperatures were measured over a large velocity range (Fig. 10) in order to access the possibility of the presence of a Zeeman pattern resulting from a possible magnetic ordering of the Eu atoms in $EuRhO_3$ and of a Zeeman pattern due to a magnetically ordered and Eu-containing impurity phase in the specimen studied. A visual inspection of these spectra shows the absence of such Zeeman patterns. As will be shown in detail below, the spectra in Fig. 10 can be fitted with a ^{151}Eu quadrupole pattern [7]. Thus, $EuRhO_3$

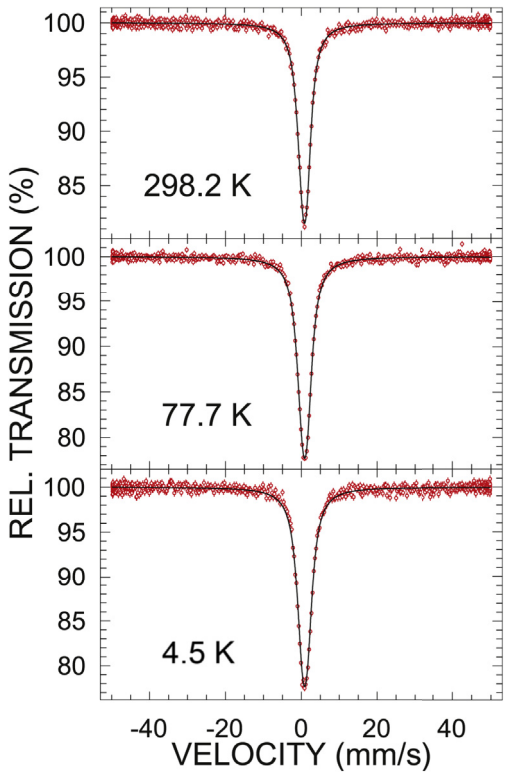

Fig. 10. ^{151}Eu Mössbauer spectra of $EuRhO_3$ at selected temperatures measured over a large velocity range and fitted (solid line) with an electric quadrupole pattern, as described in the text. The zero-velocity origin is relative to the source.

is not magnetically ordered down to 4.5 K. In addition, the value of the isomer shift δ (0.79–0.86 mm/s) corresponding to these spectra shows [7] that all Eu atoms in $EuRhO_3$ are the trivalent oxidation state, that is, there is no evidence for the presence of the Eu^{2+} ions postulated in Ref. [4].

Fig. 11 shows the Mössbauer spectra of $EuRhO_3$ at various temperatures down to 2.3 K measured over a small velocity range. The absence of any sign of a Zeeman pattern proves that the compound studied is a paramagnet down to 2.3 K. Excellent fits of the spectra can be obtained with an ^{151}Eu electric quadrupole pattern [7,14].

The temperature dependence of V_{zz} derived from the fits of the spectra in Figs. 10 and 11 is shown in Fig. 12(a). Within an experimental error, V_{zz} is practically temperature independent. This is in contrast to the Eu^{2+} compounds in which clear temperature dependence of V_{zz} is observed [15]. A weighted average of the experimental V_{zz} values in Fig. 12(a) is $0.324(8) \times 10^{22}$ V/m^2. Surprisingly, the calculated V_{zz} (Table 1) is much larger than the weighted-average value.

Fig. 12(b) displays the temperature dependence of the spectral area A obtained from the fits of the spectra in Figs. 10 and 11. The spectral area is proportional to f_a, which is expressed [7] in terms of the Debye temperature, Θ_D, as

$$f_a(T) = \exp\left\{-\frac{3}{4}\frac{E_\gamma^2}{Mc^2k_B\Theta_D}\left[1 + 4\left(\frac{T}{\Theta_D}\right)^2 \int_0^{\Theta_D/T} \frac{x\,dx}{e^x - 1}\right]\right\}, \quad (2)$$

where E_γ is the energy of the Mössbauer transition, M is the mass of the Mössbauer nucleus, and c is the speed of light. The fit of the experimental dependence $A(T)$ [Fig. 12(b)] to Eq. (2) gives $\Theta_D = 254(3)$ K. The value of Θ_D found here is close to the values of 271 K determined from the specific heat data for the $LuRhO_3$ orthorhodite [3] and of 256(1) K obtained from the ^{155}Gd Mössbauer data for the $GdRhO_3$ orthorhodite [6].

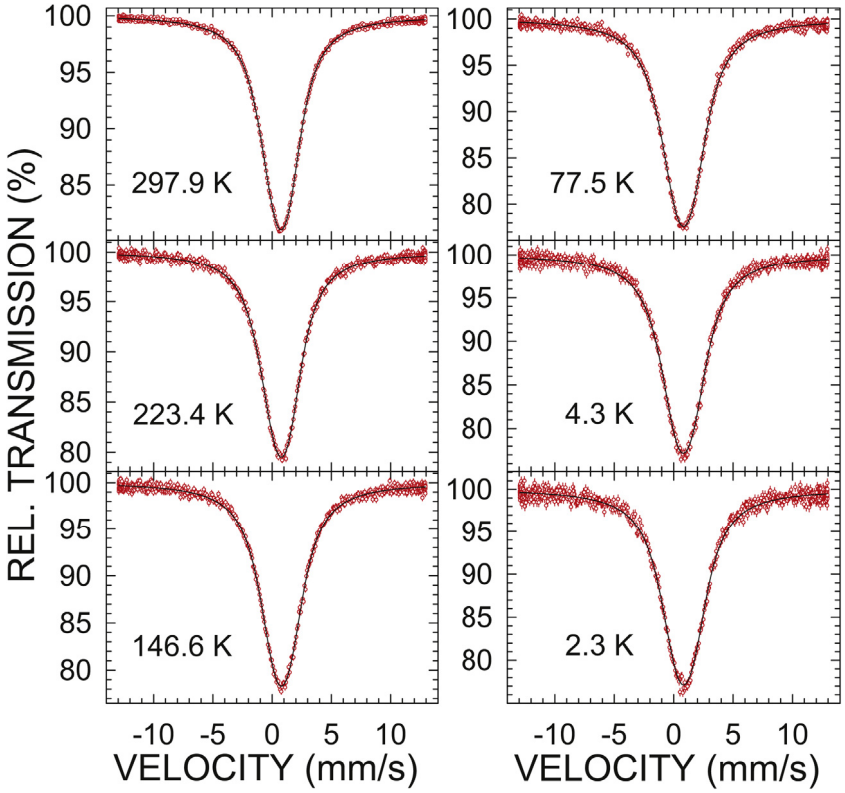

Fig. 11. ^{151}Eu Mössbauer spectra of $EuRhO_3$ at selected temperatures measured over a small velocity range and fitted (solid line) with an electric quadrupole pattern, as described in the text. The zero-velocity origin is relative to the source.

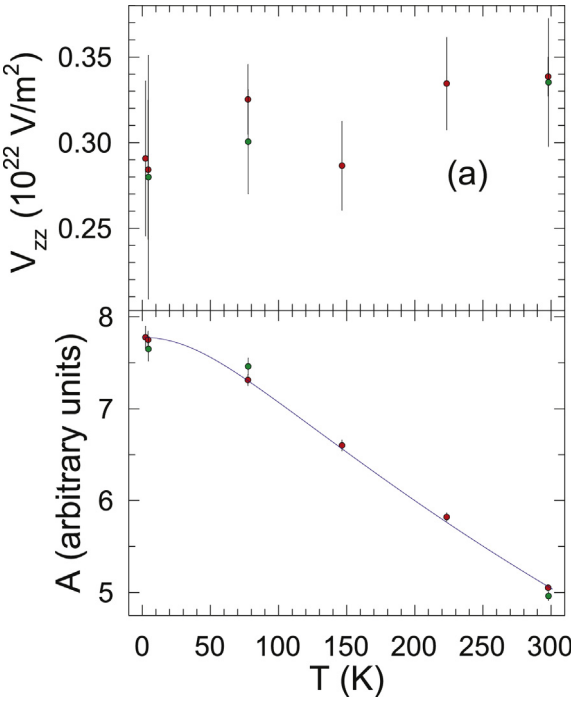

Fig. 12. Temperature dependence of (a) the principal component of the electric-field-gradient tensor V_{zz} and (b) the absorption spectral area A derived from the fits of the spectra in Figs. 10 and 11. The solid line in (b) is the fit to Eq. (2), as explained in the text.

4. Summary

We presented the results of X-ray diffraction, *ab − initio* electronic structure calculations, magnetic, and ^{151}Eu Mössbauer spectroscopy study of the $EuRhO_3$ orthorhodite. We confirmed that $EuRhO_3$ crystallizes in the orthorhombic space group *Pnma* with the lattice parameters a = 5.7499(1) Å, b = 7.6863(1) Å, and c = 5.3095(1) Å. We provided evidence for the presence of a mixture of ionic and covalent bonding in the compound studied. We presented a detailed analysis of the density of states and the energy band structure which reveals half-metallic/half-insulator characteristics of $EuRhO_3$. We found that the Eu atoms in $EuRhO_3$ are in the trivalent oxidation state. We showed that $EuRhO_3$ does not develop long-range magnetic order down to 2.3 K. We determined that the Debye temperature of $EuRhO_3$ is 254(3) K.

Acknowledgements

This work was supported by the Natural Sciences and Engineering Research Council of Canada (NSERC).

References

[1] A. Wold, B. Post, E. Banks, J. Am. Chem. Soc. 79 (1957) 6365;
A. Wold, R.J. Arnot, W.J. Croft, Inorg. Chem. 2 (1963) 972;
R.D. Shannon, Acta Crystallogr. B 26 (1970) 447;
I.S. Shaplygin, I.I. Prosychev, V.B. Lazarev, Russ. J. Inorg. Chem. 31 (1986) 1649;
V.N. Skrobot, V.L. Ugolkov, S.K. Kuchaeva, D.P. Romanov, R.G. Grebenshchikov, V.V. Gusarov, Russ. J. Inorg. Chem. 51 (2006) 1116;
R.B. Macquart, M.D. Smith, H.-C. zur Loye, Cryst. Growth Des. 6 (2006) 1361.
[2] H.S. Jarrett, A.W. Sleight, H.H. Kung, J.L. Gillson, J. Appl. Phys. 51 (1980) 3916.
[3] W. Yi, Q. Liang, Y. Matsushita, M. Tanaka, X. Hu, A.A. Belik, J. Solid State Chem. 200 (2013) 271.
[4] T. Taniguchi, W. Iizuka, Y. Nagata, T. Uchida, H. Samata, J. Alloy. Compd. 350 (2003) 24.
[5] T. Ohnishi, T. Taniguchi, A. Ikoshi, S. Mizusaki, Y. Nagata, S.H. Lai, M.D. Lan, Y. Noro, T.C. Ozawa, K. Kindo, A. Matsuo, S. Takayanagi, J. Alloy. Compd. 506 (2010) 27.

[6] F. Nejadsattari, P. Wang, Z.M. Stadnik, Y. Nagata, T. Ohnishi, J. Alloy. Compd. 725 (2017) 1098.
[7] N.N. Greenwood, T.C. Gibb, Mössbauer Spectroscopy, Chapman and Hall, London, 1971;
P. Gütlich, E. Bill, A. Trautwein, Mössbauer Spectroscopy and Transition Metal Chemistry, Springer, Berlin, 2011.
[8] M.A. Albedah, F. Nejadsattari, Z.M. Stadnik, Y. Liu, G.-H. Cao, Phys. Rev. B 97 (2018) 144426.
[9] S. Margulies, J.R. Ehrman, Nucl. Instrum. Methods 12 (1961) 131;
G.K. Shenoy, J.M. Friedt, H. Maletta, S.L. Ruby, I.J. Gruverman, C.W. Seidel, D.K. Dieterly (Eds.), Mössbauer Effect Methodology, vol. 10, Plenum, New York, 1974, p. 277.
[10] P. Blaha, K. Schwartz, G. Madsen, D. Kvasnicka, J. Luitz, R. Laskowski, F. Tran, L. Marks WIEN2k, An Augmented Plane Wave + Local Orbitals Program for Calculating Crystal Properties, Karlheinz Schwarz, Techn. Universität Wien, Austria, 2018.
[11] R.A. Young, The Rietveld Method, Oxford University Press, Oxford, 1993.
[12] J.H. Van Vleck, The Theory of Electric and Magnetic Susceptibilities, Clarendon Press, Oxford, 1932.
[13] M. Schieber, L. Holmes, J. Appl. Phys. 36 (1963) 1159.
[14] F. Grandjean, G.L. Long, G.J. Long, F. Grandjean (Eds.), Mössbauer Spectroscopy Applied to Inorganic Chemistry, vol. 3, Plenum, New York, 1989, p. 513.
[15] M.A. Albedah, K. Al-Qadi, Z.M. Stadnik, J. Przewoźnik, Solid State Commun. 613 (2014) 344.